Available online at www.sciencedirect.com
ScienceDirect
Trans. Nonferrous Met. Soc. China 35(2025) 749−764

Transactions of
Nonferrous Metals
Society of China
www.tnmsc.cn

Effect of hierarchical cell structure and internal pores on mechanical properties of thixomolded AZ91D magnesium alloy

Li-dong GU[1], Xiao-qing SHANG[1,2], Jie WANG[1], Jun-jun DENG[3], Zhen ZHAO[4], Xiao-qin ZENG[1,5]

1. National Engineering Research Center of Light Alloy Net Forming, School of Materials Science and Engineering, Shanghai Jiao Tong University, Shanghai 200240, China;
2. SJTU Paris Elite Institute of Technology, Shanghai Jiao Tong University, Shanghai 200240, China;
3. Bole Intelligent Machinery Co., Ltd., Ningbo 315801, China;
4. National Engineering Research Center of Die & Mold CAD, School of Materials Science and Engineering, Shanghai Jiao Tong University, Shanghai 200030, China;
5. State Key Laboratory of Metal Matrix Composites, Shanghai Jiao Tong University, Shanghai 200240, China

Received 18 August 2023; accepted 21 June 2024

Abstract: A comprehensive analysis of the microstructure and defects of a thixomolded AZ91D alloy was conducted to elucidate their influences on mechanical properties. Samples were made at injection temperatures ranging from 580 to 640 °C. X-ray computed tomography was used to visualize pores, and crystal plasticity finite element simulation was adopted for deformation analysis. The microstructure characterizations reveal a hierarchical cell feature composed of α-Mg and eutectic phases. With the increase of injection temperature, large cell content in the material decreases, while the strength of the alloy increases. The underlying mechanism about strength change is that coarse-grained solids experience smaller stress even in hard orientations. The sample fabricated at a moderate temperature of 620 °C exhibits the highest elongation, least quantity and lower local concentration of pores. The detachment and tearing cracks formed at lower injection temperature and defect bands formed at higher injection temperature add additional crack sources and deteriorate the ductility of the materials.

Key words: AZ91D magnesium alloy; fabrication technology; cell structure; pores; strength; ductility

---

1 Introduction

Magnesium alloys, with their low density, possess distinct advantages in weight savings. Through alloying to enhance strength, magnesium alloys have the potential to become lightweight components for consumer electronics, bicycles, and drones [1−3]. Especially, for the current booming field of new energy vehicles, magnesium alloys have vast application prospects. Magnesium alloys are typically fabricated through casting. However, casting is a high energy consumption technology with the process of heating metals to the liquid state. Compared with casting, the semi-solid processing technique provides an efficient and energy-saving manufacturing method [4]. It compensates for some drawbacks of die casting and can produce materials with excellent mechanical properties [5]. As reported by OKAYASU and FUKUI [6], the Mg−9.0Al−0.8Zn alloy fabricated via thixomolding had superior mechanical properties than the one made by cold-chamber die casting or hot-chamber die casting. Additionally, higher fatigue strength and

---

Corresponding author: Xiao-qing SHANG, Tel: +86-18317039626, E-mail: xqshang@sjtu.edu.cn;
Xiao-qin ZENG, Tel: +86-21-54742301, E-mail: xqzeng@sjtu.edu.cn

DOI: https://doi.org/10.1016/S1003-6326(24)66712-9

1003-6326/© 2025 The Nonferrous Metals Society of China. Published by Elsevier Ltd & Science Press
This is an open access article under the CC BY-NC-ND license (http://creativecommons.org/licenses/by-nc-nd/4.0/)

higher crack growth resistance were realized with thixomolding. MATHIEU et al [7] reported that the AZ91 alloy made by semi-solid casting possessed a corrosion rate 35% lower than the one made by die casting.

Thixomolding is a kind of semi-solid technology, which involves heating metals from the solid state to the semi-solid temperature, and breaking down dendrites through stirring. This process ensures the uniform distribution of spherical, equiaxed, and fine primary phases within the liquid phase [8]. Through heating the barrel and rotation of the screw, metal chips are continuously transported forward and gradually transformed into a semi-solid slurry with thixotropic features [9]. The slurry is then injected into the mold with high-speed to form the product. The entire process is sealed, and the material is controlled in a semi-solid state without achieving complete melting. Besides, the thixomolding process does not require protective gas. Therefore, thixomolding emerges as a green technology featured with safe, environmentally friendly, and efficient production process. Additionally, thixomolding technology gives easy access to fabricating metal composite [10−12].

The microstructure of thixomolded AZ91D alloy is composed of spheroidal α-Mg and network-like eutectic structures [13]. Based on the characteristics of thixomolding, primary solid naturally exists in the materials. The amounts of primary solids greatly affected the mechanical performance [14]. With a solid fraction below 20%, the internal primary solid and the eutectic structures determined the properties; as the un-melted fraction became higher, the interface between matrix and eutectic mixture played a dominant role [15]. The change of thixomolding technology induces microstructure changes [16]. According to previous studies [14,15], the best properties were obtained when barrel temperature and shot velocity were the highest. When the barrel temperature was increased, the solid fraction was decreased, the grain was refined, and the material got higher microchemical and microstructure homogeneity [15].

Solidification defects form during the thixomolding process [17,18], and the barrel temperature affects the formation of porosity. When the slurries were heated to a full liquid state, the melt flow would approach turbulent mode [19,20], and the possibility of porosity formation was increased. Solidification defects generally have irregular shapes. LI et al [20] conducted a detailed analysis about the defect formation mechanism of AZ91D alloy in die casting, and identified two kinds of defects: the porosity in defect band was related to melt flow and had characteristics of stitching seamlessly; while shrinkage pore was induced by solidification contraction and randomly located at grain boundaries. Defects determine the failure of metallic materials [21,22]. As reported by LI et al [23], crack initiated at the gas shrinkage pore in die casting AM60B magnesium alloy with less externally solidified crystal (ESC); while for the material with large and complex ESCs, defect band acted as crack initiation region. For the analysis of internal defects, the non-destructive technique micro-computed tomography (XCT) provides an efficient experimental methodology [24,25]. AZGHANDI et al [26] conducted an in-situ XCT experiment to determine the pore evolution of AZ31 alloy during plastic deformation, and revealed the slower rate of pore growth in the fine-grained materials.

In summary, the cell structure of thixomolded magnesium alloy is distinct from the ones made by casting [27]. In addition, due to the variation of flow characteristics of fluid in casting and thixomolding, the pore features in materials made by the two technologies are different. Till now, most studies referring to the AZ91 alloy are for the cast material, while the understanding about microstructure and pore features of the thixomolded magnesium alloy is still superficial. This work examines and analyzes the cell structure, the characteristics of pores, and their changes with the injection temperature of a thixomolded AZ91D alloy. Focus is laid on the underlying cause of the strength change with the fraction of primary α-Mg solids, and the internal correlation between ductility and pore formation mechanism.

2 Experimental

Thixomolding was conducted in a specialized machine of BL300MG with a short nozzle from BOLE Intelligent Machinery Co., Ltd., Ningbo, China. The principle and process of the thixomolding technology are shown in Fig. 1(a). Raw chips were cut from a commercial AZ91D billet into sizes of 1.2 mm × 1.2 mm × 4 mm. The

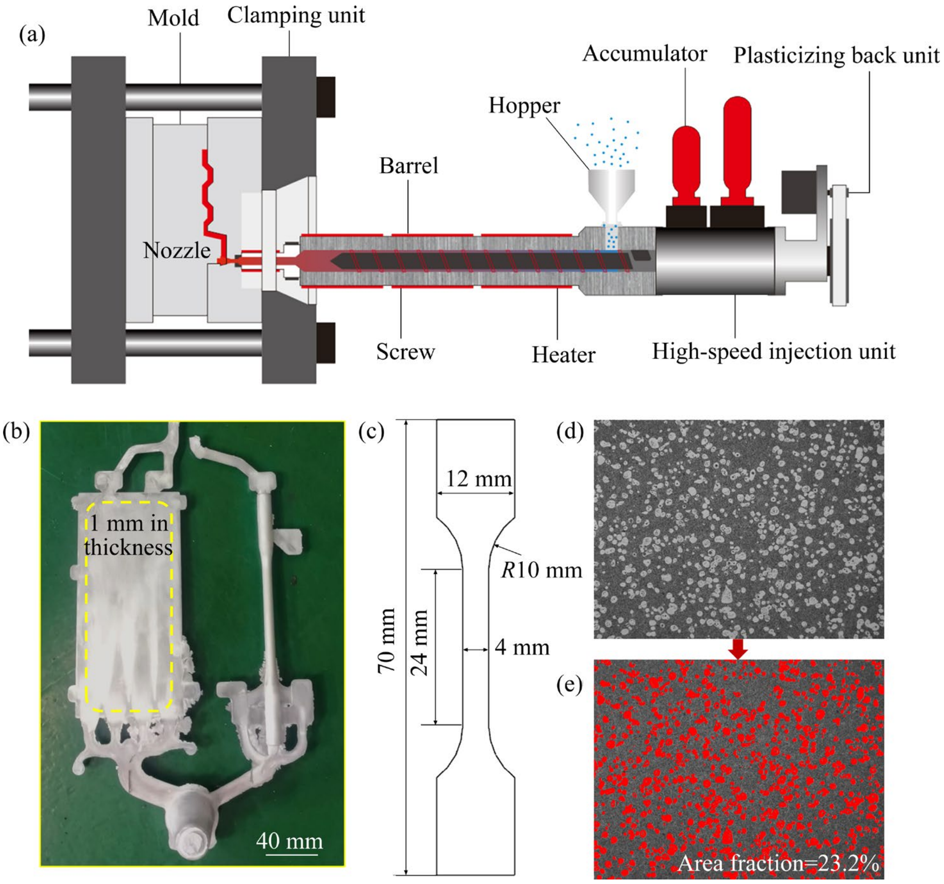

Fig. 1 Thixomolding technology and product: (a) Schematic diagram of thixomolding equipment and process; (b) Thixomolded product; (c) Shape and dimension of tensile sample; (d) Metallographic result of sample fabricated at 590 °C; (e) Statistical analysis of primary solid

chips were put into the machine through the hopper, transported forward in the barrel with a semi-solid state, and injected into the mold to form the product. The die temperature was held at 200 °C; the screw rotation rate and injection velocity were fixed at 100 r/min and 3.0 m/s, respectively. Seven different injection temperatures were employed: 580, 590, 600, 610, 620, 630 and 640 °C.

The thixomolded product is presented in Fig. 1(b). The chemical composition of the material was measured by ICP and determined as Mg−9Al−0.75Zn (wt.%). The plate product had a thickness of 1 mm. Samples for tensile test, microstructure and XCT examinations were cut from the plate. The shape and dimension of the sample for tensile test are shown in Fig. 1(c). The tensile velocity was set to be 1 mm/min, which yielded a strain rate in the gauge region lower than 10^{-3} s^{-1}. Three parallel tests were conducted for each temperature condition, and the 0.2% yield stress, tensile stress, and elongation to failure were obtained based on the average of three tests. Statistical analysis of the primary solid fraction was performed based on image recognition of the metallographic characterization, and a representative result for the 590 °C condition is shown in Figs. 1(d) and (e).

A flowability test was conducted by using a specially designed mold and the results are shown in Fig. 2. With the increase of injection temperature, the flowability becomes better, manifested as the increase of fluidity length. Meanwhile, the solid fraction is decreased. Table 1 lists quantitative data of the area fraction of primary solid fraction under different injection temperature conditions. At 580 °C, the fraction of primary solid reaches 43.8%. The decrease of primary solid amount is evident at lower temperatures from 580 to 610 °C. At 610 °C, the solid fraction is decreased to 5.1%. Further increase of the injection temperature induces a small change of the primary solid fraction. When the injection temperature is increased to 630 °C, the primary solid content becomes very low, and the fluidity of the slurry is close to liquid.

Scanning electron microscopy (SEM), energy

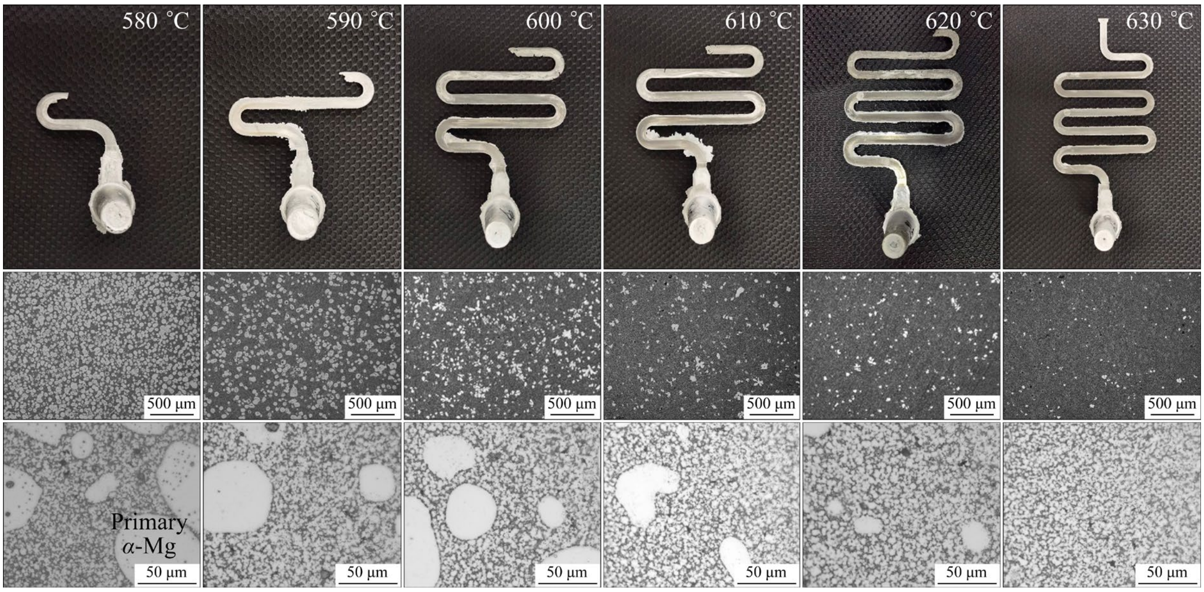

Fig. 2 Fluidity test results and optical micrographs of thixomolded AZ91D alloy made at injection temperatures ranging from 580 to 630 °C

Table 1 Area fraction of primary solid under different injection temperature conditions

Temperature/°C	580	590	600	610	620	630	640
Area fraction of solid/%	43.8	23.2	10.2	5.1	4.3	1.4	1.1

dispersive spectrometer (EDS), and electron backscatter diffraction (EBSD) characterizations were conducted to determine the microstructure, chemical component, as well as the grain structure. Step size used for EBSD was 0.15 μm. Internal pores formed during the thixomolding process were examined by an X-ray computed tomography scanner (Xradia 520 Versa). Voxel resolution employed in the XCT examinations was 0.9 μm. With the consideration that a detectable damage feature had three voxels in each direction, pores with volume larger than $27\times(0.9\ \mu\text{m})^3=19.683\ \mu\text{m}^3$ were recognized. Every XCT result involved 100 two-dimensional slices, and the three-dimensional solid was re-constructed from the slices. The pore connectivity was determined in the way that voxels in the three-dimensional XCT images were related to their neighbors. A set of connected voxels constitute an individual void.

Full-field crystal plasticity finite element simulations were conducted in parallel to determine the deformation characteristics [28]. The rate-dependent constitutive formulations proposed by SALEM et al [29] were utilized to describe the slip and twinning behaviors. A power-law formulation was employed to represent the shearing rate of slip. The plastic velocity gradient ($\boldsymbol{L}_0^{\mathrm{p}}$) and slip shearing rate ($\dot{\gamma}_{\mathrm{sl}}^{\alpha}$) are expressed as follows:

$$\boldsymbol{L}_0^{\mathrm{p}}=\left(1.0-f_{\mathrm{tw}}\right)\sum(\dot{\gamma}_{\mathrm{sl}}^{\alpha}\boldsymbol{S}_{\mathrm{sl}}^{\alpha})+f_{\mathrm{tw}}\sum(\dot{\gamma}_{\mathrm{tw}}^{\beta}\boldsymbol{S}_{\mathrm{tw}}^{\beta})+ f_{\mathrm{tw}}\sum(\dot{\gamma}_{\mathrm{sl}}^{\alpha}\hat{\boldsymbol{S}}_{\mathrm{sl}}^{\alpha}) \tag{1}$$

$$\dot{\gamma}_{\mathrm{sl}}^{\alpha}=\dot{\gamma}_{\mathrm{sl}}^{0}\left|\frac{\tau_{\mathrm{sl}}^{\alpha}}{g_{\mathrm{sl}}^{\alpha}}\right|^{1/m_{\mathrm{sl}}}\mathrm{sign}(\tau_{\mathrm{sl}}^{\alpha}) \tag{2}$$

where $\boldsymbol{S}_{\mathrm{sl}}^{\alpha}$, $\hat{\boldsymbol{S}}_{\mathrm{sl}}^{\alpha}$ and $\boldsymbol{S}_{\mathrm{tw}}^{\beta}$ are the Schmid tensors of slips for the untwinned matrix, twinned matrix, and the twinning systems, respectively; $\dot{\gamma}_{\mathrm{sl}}^{\alpha}$ and $\dot{\gamma}_{\mathrm{tw}}^{\beta}$ denote the plastic shearing rates of the α slip system and the β twinning system, respectively; f_{tw} is the volume fraction of twinning; $\dot{\gamma}_{\mathrm{sl}}^{0}$ is the reference shear rate; $\tau_{\mathrm{sl}}^{\alpha}$ is the resolved shear stress of α slip; g_{sl}^{α} is the slip resistance; m_{sl} is the rate sensitivity parameter. Activations of basal, prismatic, pyramidal $\langle a\rangle$, and pyramidal $\langle c+a\rangle$ slips were considered, and the critical resolved shear stresses for the slip systems were set to be 12, 38, 36 and 60 MPa, respectively [30].

3 Results

3.1 Change of mechanical properties with injection temperature

The tensile stress−strain curves of the thixomolded material fabricated at different injection temperatures are shown in Fig. 3(a). The yield strength, ultimate tensile strength, and fracture elongation are listed in Table 2, and their changes with injection temperature are exhibited in Fig. 3(b). The mechanical properties indicate that the yield stress of AZ91D alloy produced by thixomolding increases monotonically with the increase of injection temperature. The sample made at 640 °C gets a maximum yield strength of 175 MPa. The elongation, on the other hand, does not follow a monotonic trend with injection temperature. The sample made at 620 °C gets the maximum elongation of 7.2%. The change of strength and ductility will be discussed in terms of microstructure and internal defects.

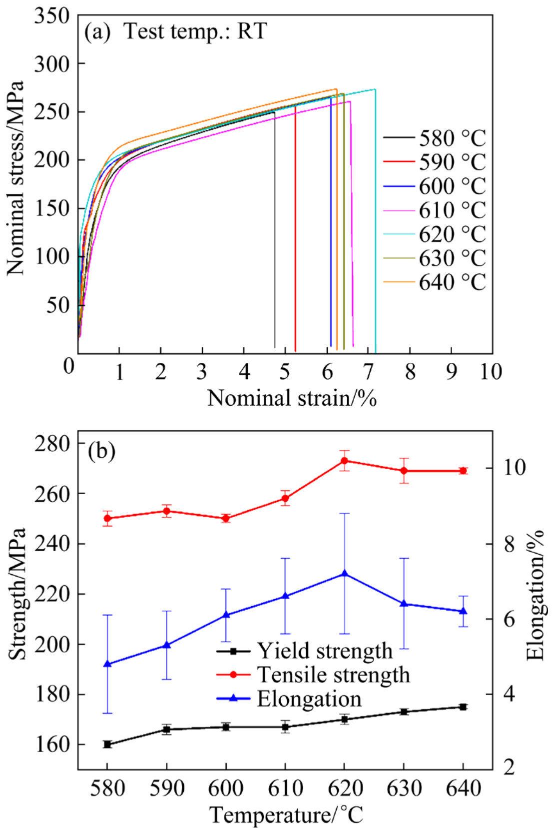

Fig. 3 Mechanical properties of thixomolded AZ91D alloy: (a) Stress−strain curves; (b) Change of strength and elongation with injection temperature

Table 2 Yield strength, tensile strength and elongation of thixomolded AZ91D alloy at different injection temperature

Temperature/°C	Yield strength/MPa	Ultimate tensile strength/MPa	Elongation/%
580	160±1.4	250±3.0	4.8±1.3
590	166±2.0	253±2.5	5.3±0.9
600	167±1.6	250±1.6	6.1±0.7
610	167±2.5	258±3.0	6.6±1.0
620	170±2.1	273±4.0	7.2±1.6
630	173±1.2	269±5.0	6.4±1.2
640	175±0.8	269±1.2	6.2±0.4

3.2 Cell structure of thixomolded AZ91D alloy

Figure 4 presents the SEM results of the thixotropic microstructures of AZ91D alloy fabricated at different injection temperatures. The thixomolded material presents a cellular structure with α-Mg matrix decorated by eutectic component. Large cell is composed of primary coarse-grained α-Mg and eutectic phase, and small cell is characterized by fine-grained α-Mg formed during solidification and the eutectic component. There is a slight change of the eutectic phase distribution with temperature. For lower injection temperature conditions of 590 and 620 °C, the cells distribute uniformly in the material; while for the sample made at higher temperature of 640 °C, the microstructure becomes more heterogeneous, as represented by some regions that are rich in the eutectic component, while the others mainly consist of the α-Mg matrix. The cellular characteristics of materials produced by thixomolding have similarities with the one fabricated by additive manufacturing [31] since both technologies represent rapid-cooling non-equilibrium solidification process.

The major chemical elements of Mg, Al and Zn were detected by EDS, and the elemental maps are presented in Fig. 5. From the chemistry characterization, it is clear that the eutectic component is rich in Al. This phase is not necessary to be the equilibrium phase $Mg_{17}Al_{12}$ since thixomolding is a rapid non-equilibrium solidification process. The amount of $Mg_{17}Al_{12}$ identified by EBSD in Fig. 6 is less than the intermetallic compound identified by SEM characterization in Fig. 4. A fluctuation of Al and Mg inside matrix and the eutectic phase is shown, which indicates the inhomogeneous distribution of chemical components.

3.3 Influence of injection temperature on grain size and texture

The material made by thixomolding technology

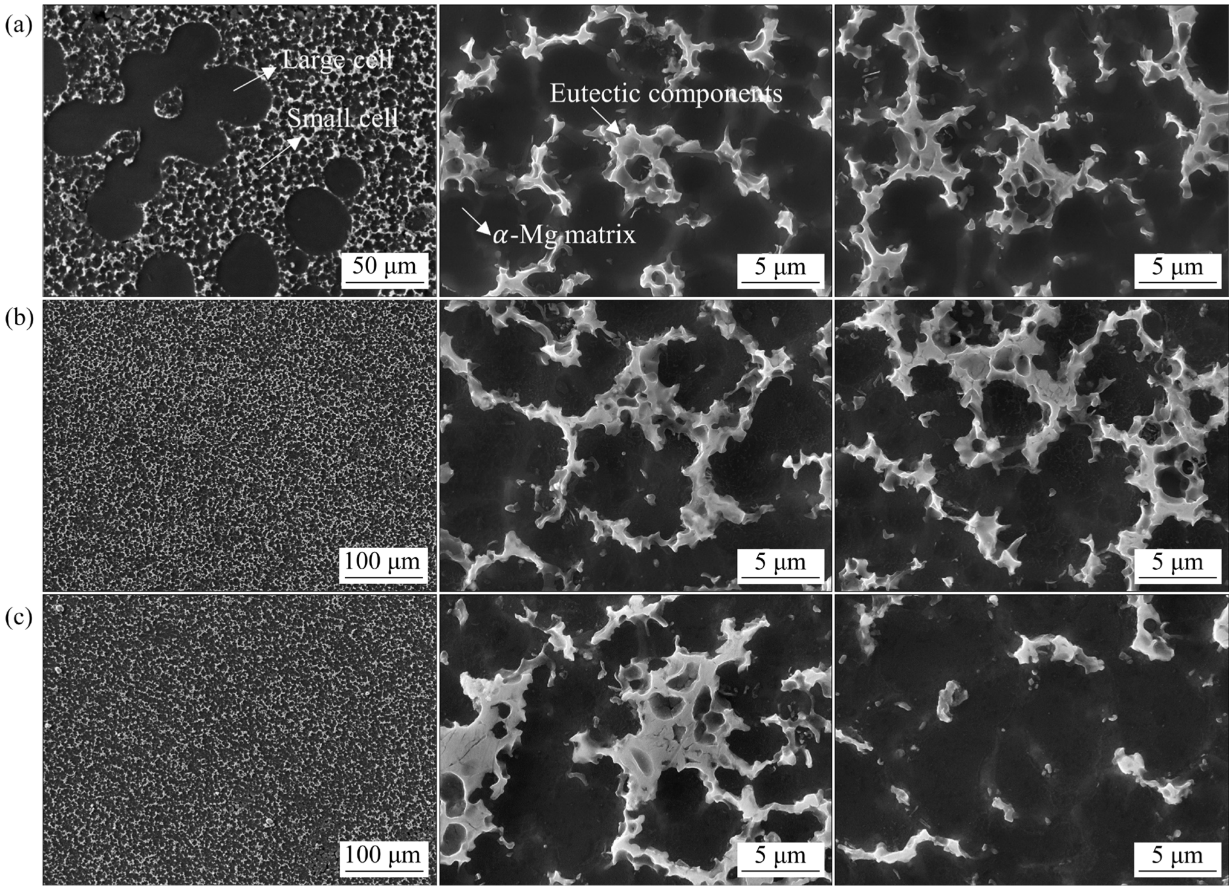

Fig. 4 SEM images of cellular structure composed of α-Mg and eutectic components of AZ91D alloys fabricated at different injection temperatures: (a) 590 °C; (b) 620 °C; (c) 640 °C

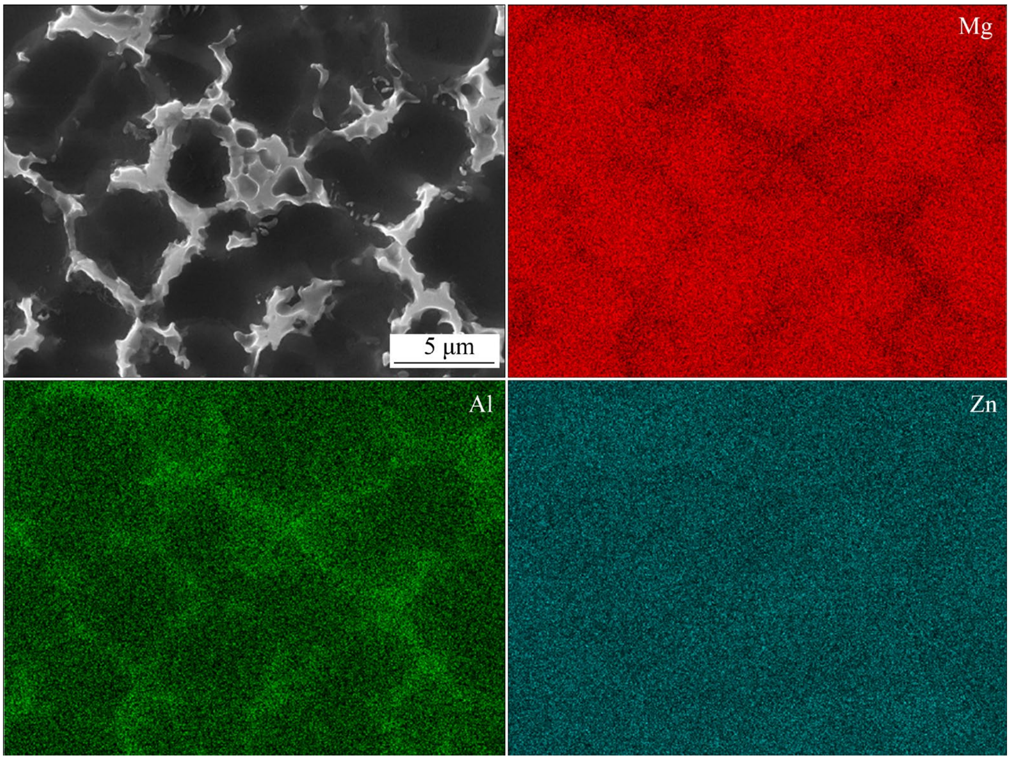

Fig. 5 EDS elemental maps of Mg, Al and Zn for sample fabricated at injection temperature of 620 °C

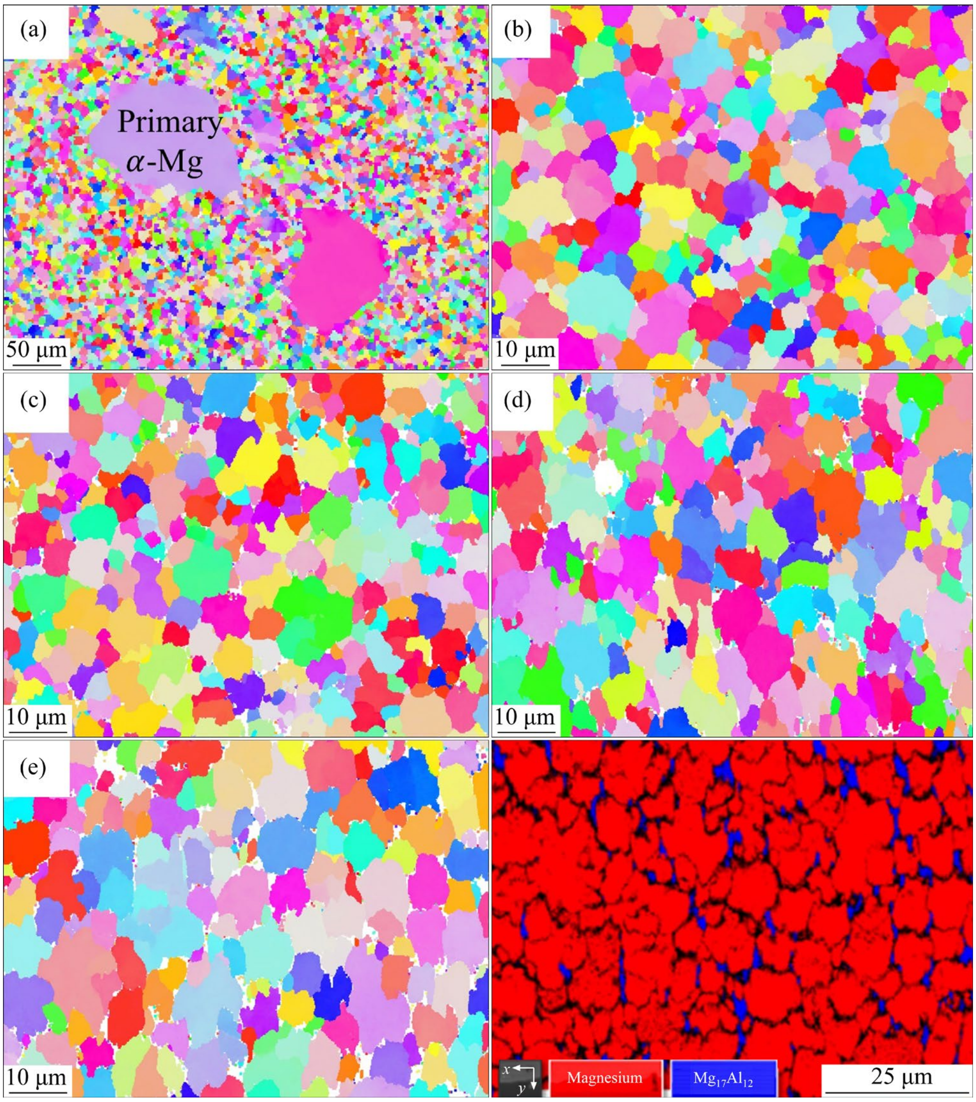

Fig. 6 EBSD orientation maps of thixotropic microstructures for samples made at different injection temperatures: (a, b) 580 °C; (c) 600 °C; (d) 620 °C; (e) 640 °C

has equiaxial grains, as shown in the EBSD orientation maps in Fig. 6. From Fig. 6(a), it is identified that the thixomolded AZ91D alloy exhibits a mixed grain structure: the primary α-Mg solids have larger grain size while the solidification matrix has fine grains. Table 3 shows the average grain sizes for solidification zone at different injection temperatures. The smallest grain size of 4 μm is obtained in the 600 °C injection temperature scenario. The primary α-Mg has grain size larger than 100 μm and behaves as coarse grain in the mixed-grain material. In the thixotropic microstructure, grains do not have a typical hexagonal morphology. Grains in the material made at lower temperatures of 580 and 600 °C present a roughly spherical or ellipse shape. While for the sample made at higher injection temperatures of 620 and 640 °C, its grains have an elongated feature. From the phase map in Fig. 6(e), equilibrium phases of $Mg_{17}Al_{12}$ are recognized.

Table 3 Average grain sizes for solidification zone in thixomolded AZ91D alloy fabricated at different injection temperatures

Temperature/°C	580	590	600	620	640
Average grain size/μm	6.0	7.0	4.0	4.5	4.5

The $\{0001\}$ and $\{10\bar{1}0\}$ pore figures of AZ91D alloy fabricated at different injection temperatures are shown in Fig. 7. Via combining the results of orientation distribution map and pore

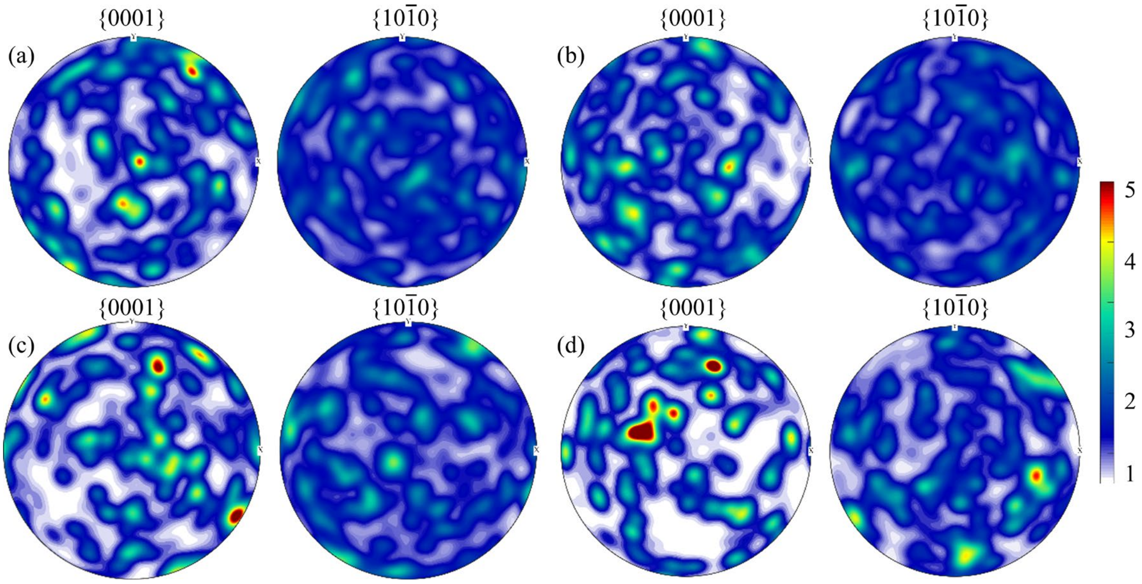

Fig. 7 {0001} and {10$\bar{1}$0} pore figures for samples fabricated at different injection temperatures: (a) 580 °C; (b) 600 °C; (c) 620 °C; (d) 640 °C

figures, it is determined that the thixomolded alloy has a weak texture. The pore figures show high pole intensity in local regions, which indicates preferred grain orientations. At 640 °C, larger regions with high pore density appear. However, since the high-intensity poles are limited in number and have a dispersed distribution, the material still exhibits an overall weak texture. The influence of injection temperature on texture is not significant.

3.4 Characteristics of internal pore and fractographs of thixomolded AZ91D alloy

Internal defects of the thixomolded AZ91D magnesium alloys were carefully examined by the XCT technique. Three-dimensional solid was reconstructed from two-dimensional slices and the defect was recognized by its grey level variation with matrix. Figure 8 displays the distribution of pores in the solid and the representative two-dimensional slices for the samples fabricated at 590, 620 and 640 °C. Table 4 shows quantitative data involving the pore volume fraction (PVF), pore number and average pore volume. The thixomolded AZ91D alloy made at 640 °C gets the largest number of independent pores; its pore number reaches 20104. The sample fabricated at 620 °C has 12866 internal pores, which is the smallest among the tested cases. The morphology of the largest three defects is shown in Fig. 9. The accurate recognition of large pores from XCT can be confirmed by the comparison with SEM results. From the SEM characterizations of the fracture surface in Figs. 10 and 11, it is determined that most pores have diameter of several micrometers, and the larger ones possess diameter larger than 20 μm. This data coincides with the XCT measurement in that the two-dimensional cutting slice of pores from the three-dimensional XCT is at this size scale. Therefore, the method of pore recognition from XCT is reasonable.

All the defects possess irregular shapes with a lot of bifurcations and small facets. Dendritic features present all over the surfaces of the defects. The large pores in the 590 °C condition have a larger length/width ratio, which denotes a thin and long shape. Pores formed at 620 °C have smoother free surfaces than those formed at 590 and 640 °C. The largest pore with a volume of 21064 μm^3 appears at 590 °C. The volume of the largest pore at 620 °C is only half of that formed at 590 °C. The presence of the largest pore represents a local concentration, and it is generally believed that larger pores have a greater impact on plasticity and ductility. The variation of pore number, morphology and volume manifests the non-negligible effect of injection temperature on formation mechanism of pores.

The fractographs of the thixomolded samples shown in Fig. 10 denote a discontinuous fracture feature with plenty of small facets and tearing edges. The fracture surface is perpendicular to the tensile direction and has a transgranular characteristic. The fracture feature manifests a combined brittle and

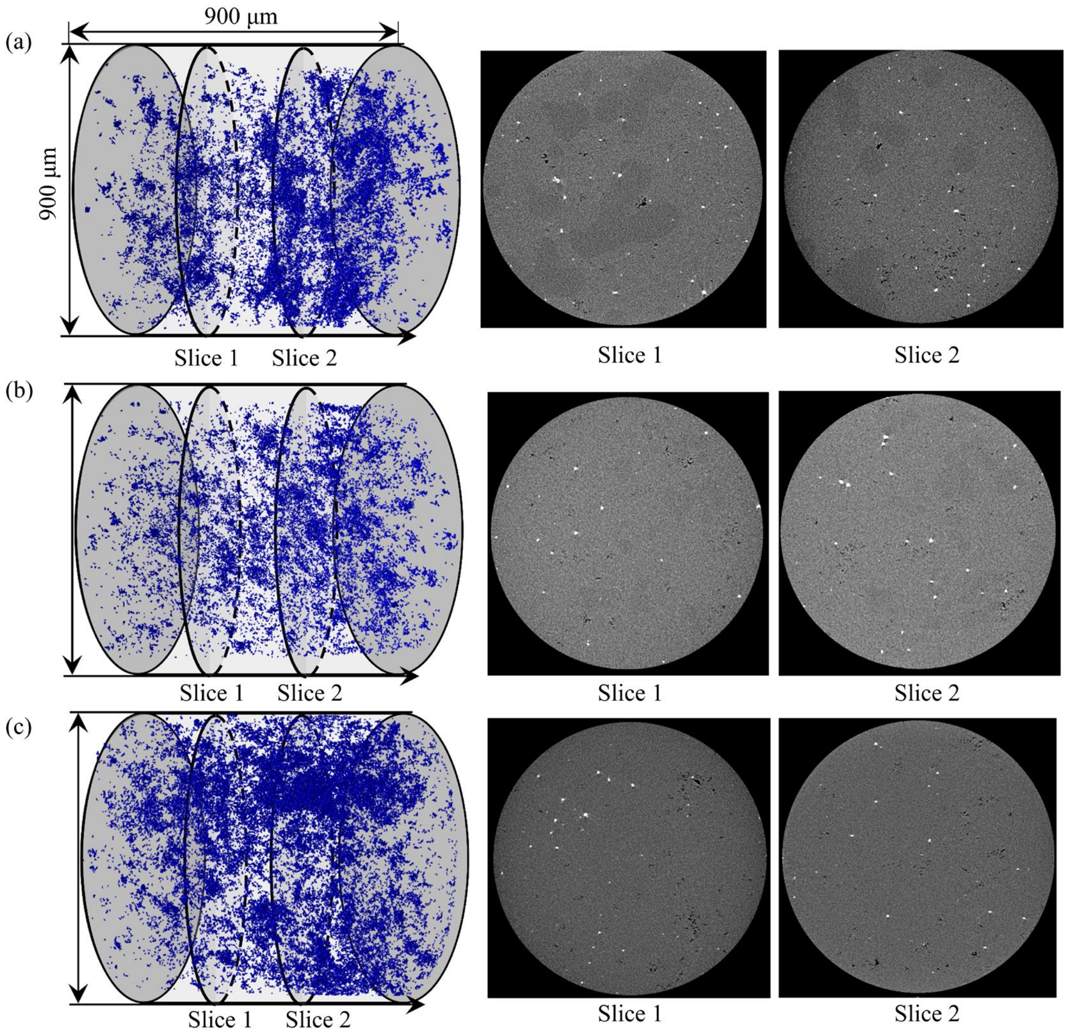

Fig. 8 XCT results of three-dimensional pore distribution and representative two-dimensional slices at different injection temperatures: (a) 590 °C; (b) 620 °C; (c) 640 °C

Table 4 Quantitative pore data of PVF, pore number and average pore volume

Temperature/°C	PVF in whole solid/%	Max PVF in slice/%	Volume of largest pore/μm^3	Number of pores	Average pore volume/μm^3	Equivalent pore radius/μm
590	0.33	0.86	21064	15744	97.84	2.86
620	0.25	0.55	10041	12866	85.70	2.73
640	0.41	0.76	15657	20104	104.78	2.92

ductile fracture mode of quasi-cleavage fracture [32]. This kind of fracture initiates with the formation of a large number of small cleavage cracks, which correspond to the high-density small facets; these facets denote the brittle aspect of the fracture. The cracks would grow locally during plastic deformation and finally coalesce in a ductile manner, forming the ductile tearing edge. The presence of some large tearing edges at 620 °C indicates more contributions made by ductile damage in the final failure; this result coincides with better ductility in the scenario. At 640 °C, pores induced by lack of fusion are observed.

4 Discussion

4.1 Influence of injection temperature on defect formation mechanism

Emphasis was paid to the formation mechanism of internal defects in the thixomolded magnesium alloys. Figure 11 displays representative pores formed in different temperature conditions.

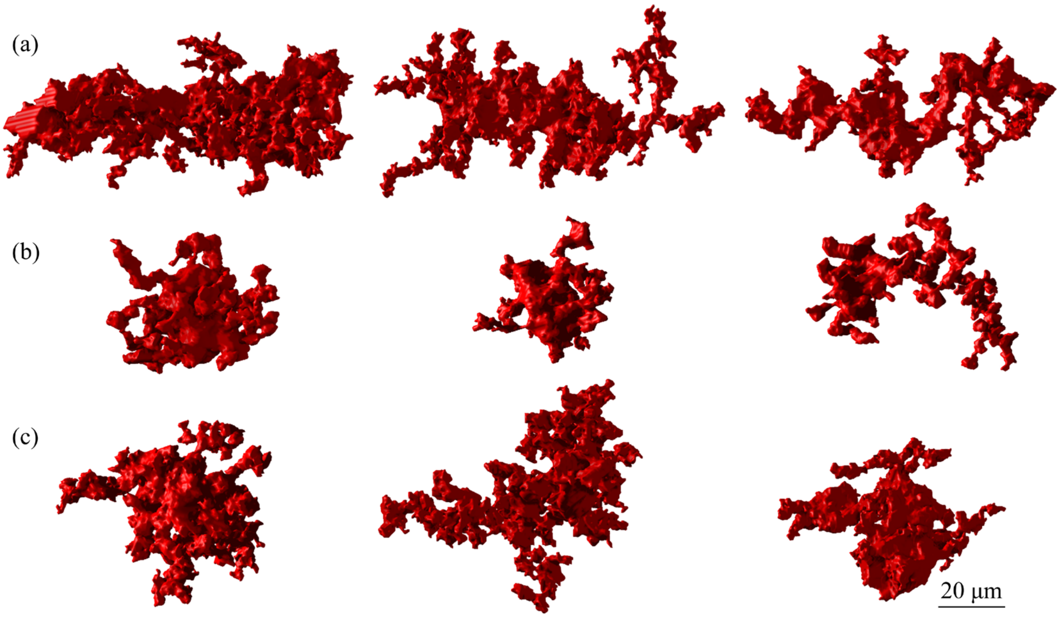

Fig. 9 Largest three pores recognized by XCT in samples fabricated at different injection temperatures: (a) 590 °C; (b) 620 °C; (c) 640 °C

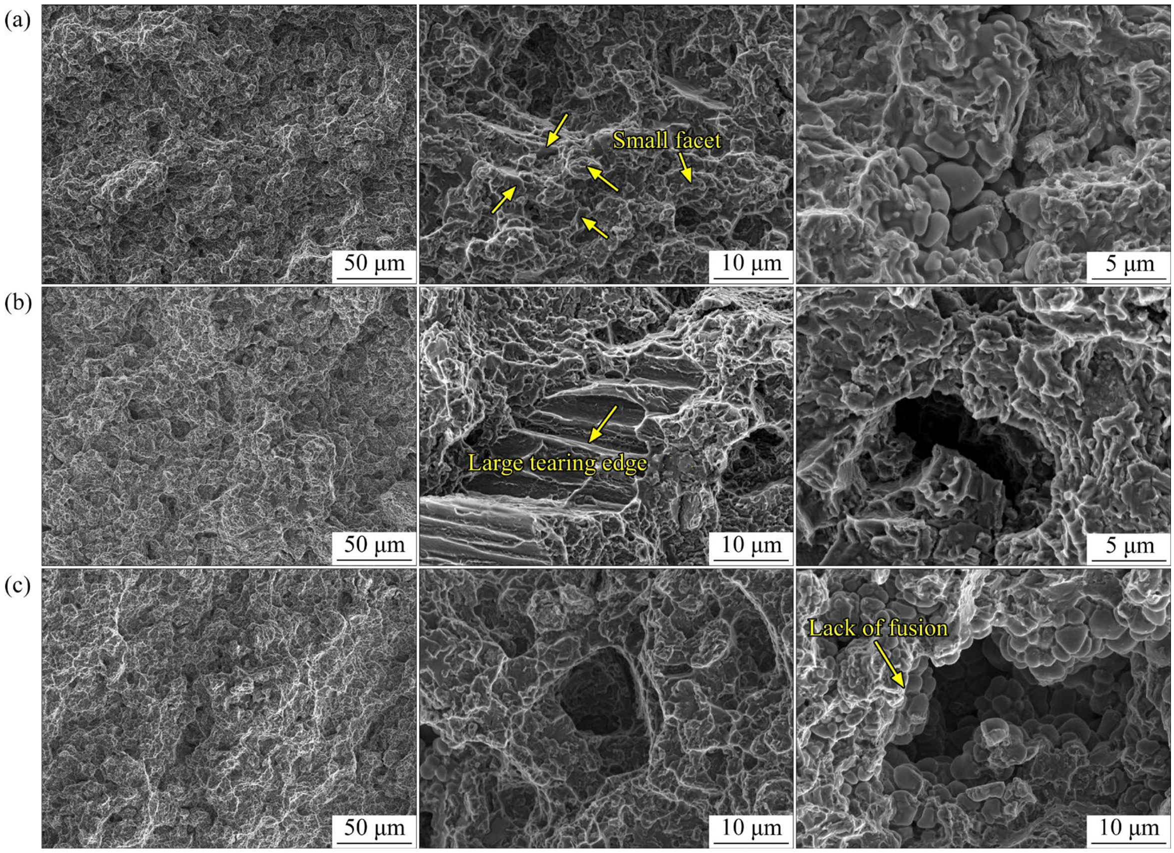

Fig. 10 Fractographs of thixomolded AZ91D alloys made at different injection temperatures: (a) 590 °C; (b) 620 °C; (c) 640 °C

The major kind of defects in the thixomolded materials is shrinkage pores. They widely distributed in samples fabricated at injection temperatures from 590 to 640 °C. Defects such as detachments, tearing cracks and defect bands also appear. Under lower injection temperature conditions of 580−620 °C, the

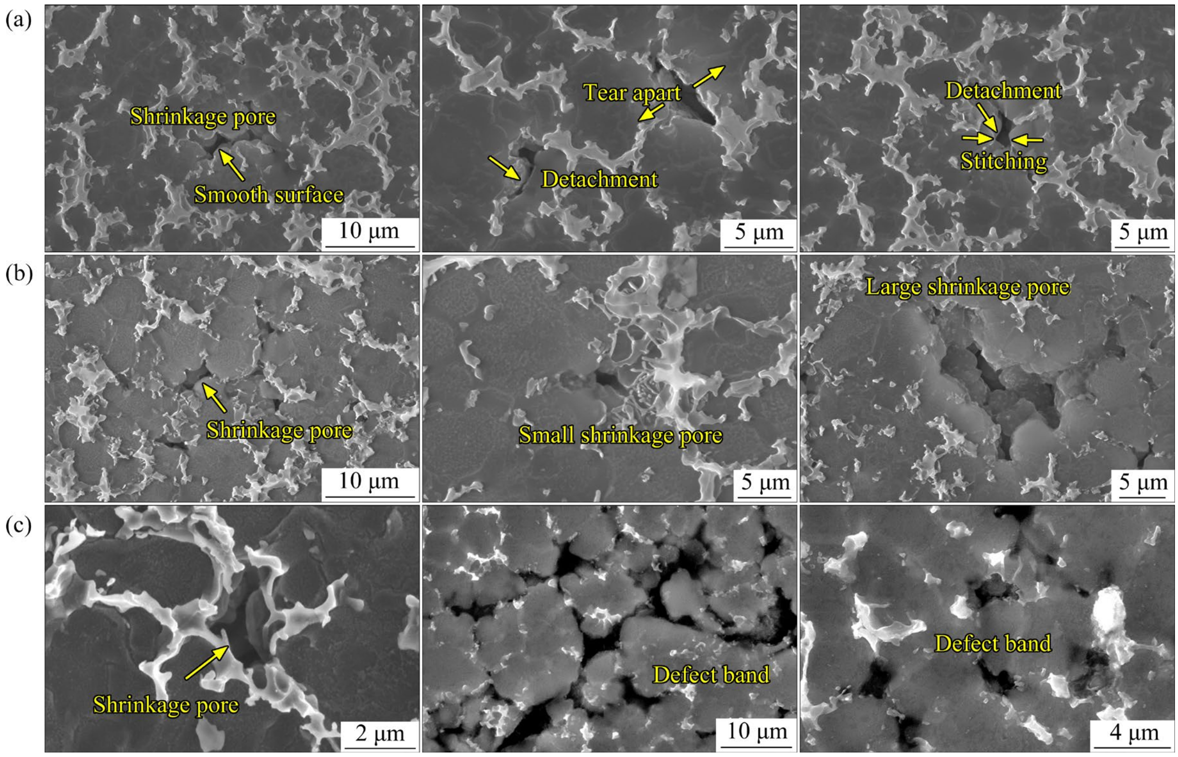

Fig. 11 SEM images showing representative pores at different injection temperatures: (a) 590 °C; (b) 620 °C; (c) 640 °C

slurry has a higher solid phase fraction and possesses thixotropic feature. In tandem with this, the pore formation and ductility are dependent on the primary solid fraction. Too many solids manifest a poor ability of the fluid to feed pores [16]. Representative results about the defect formation in the high solid fraction condition are given in Fig. 11(a). With the higher liquid viscosity and poor liquidity, adjacent solid crystals which flow with different rates or directions would induce large local stress and tear the materials apart, leading to the formation of lathy tearing defects. Another defect type identified for the low injection temperature condition is detachment; two sides of this kind of crack can be stitching seamlessly [20]. In summary, the tearing crack and detachment related to the high slurry viscosity at lower injection temperature provide additional defect sources.

Defect bands generate in the sample made at 640 °C, as shown in Fig. 11(c). Defect band is featured with a larger number of irregular pores in local regions [21,33]. With higher injection temperature, the solid phase fraction becomes very low, and the slurry fluidity has liquid features. The filling process is thus similar to casting. It is known that a large number of pores and the defect bands featured with independent pores are generated during casting due to the turbulent melt flow [21]. Therefore, the sample made at a higher injection temperature of 640 °C gets the largest number of independent pores. For the AZ91D alloy made at a moderate temperature of 620 °C, shrinkage pores constitute the majority of internal defects, as confirmed by the SEM observations of pores in Fig. 11(b) as well as the XCT results of defect with smooth surface in Fig. 9. In summary, apart from shrinkage pores, materials made at 590 and 640 °C get other kinds of defect formation origins.

Quantitative analysis of pore was performed in terms of the PVF, pore size and local concentration. From the quantitative data in Table 4, it is known that the alloy made at 640 °C has the maximum PVF in whole solid and the largest pore number. However, the sample does not get the worst ductility: its elongation is 6.2%, which is larger than 5.3% of the one made at 590 °C. This result indicates that the fraction of internal defects is not the sole controller of ductility. To clarify the defect-dependent ductility, the local concentration of pores should also be taken into account. A direct measurement of local pore concentration is the PVF of slices. By using a resolution of 0.9 μm in the XCT tests, every slice gets a volume of 0.57 μm^3. The pore volume fraction in slices was calculated.

The sample fabricated at an injection temperature of 590 °C gets the largest slice PVF of 0.86%, which manifests the severest pore concentration. Meanwhile, the smallest elongation presents in the scenario. The 640 °C sample gets a relatively large slice PVF of 0.76%. Moderate processing temperature of 620 °C is beneficial to inhibiting pore formation and concentration. The maximum slice PVF is reduced to 0.55% in the 620 °C thixomolded sample, and the elongation is increased to 7.2%. Given that both the elongation and suppression of local pore concentration have a decreasing sequence of 620 °C sample > 640 °C sample > 590 °C sample, it is concluded the ductility is closely related to local defect concentration.

4.2 Influence of hierarchical cell structure and initial pores on mechanical properties

With the increase of injection temperature from 580 to 640 °C, the yield strength of the thixomolded AZ91D alloy increases monotonically. This phenomenon can be elucidated by considering the change of hierarchical cell structure feature with temperature. At lower injection temperatures, primary α-Mg solids with larger grain size exist. The coarse-grained cells constitute large and soft phase in the material. The results shown in Fig. 12 present a negative relationship between yield strength and the fraction of primary α-Mg.

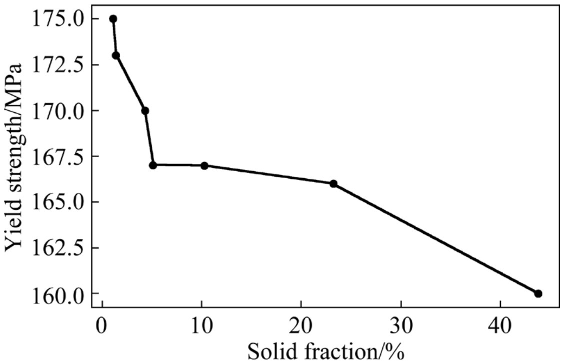

Fig. 12 Correlation between yield strength and fraction of primary coarse-grained solid

The underlying mechanism about strength change with the coarse-grained primary solid content was delved into through the identification of meso-scale deformation feature [34]. For this purpose, simulations based on the crystal plasticity finite element method (CPFEM) were conducted. A CPFEM model was built based on the EBSD data, as shown in Figs. 13(a) and (b). Both coarse and fine grains are involved in the microstructure, and the CPFEM model represents the grain morphology and hierarchical grain structure. The experimental grain orientation is also considered in the simulation via adopting the Euler angles from EBSD in the modeling. Internal pores are not included in the CPFEM model since introducing discontinuous features in a simulation method within continuum mechanics framework has some difficulties.

The simulated results of von Mises stress, accumulated shear strain, and strains for basal and non-basal slips are presented in Figs. 13(c−f). Stress hot spots appear as a dispersed distribution in fine grains in the RVE, as shown in Fig. 13(c). The strain distribution in Fig. 13(d) indicates the formation of multiple shear bands inclined to the tensile direction. This meso-scale deformation feature is consistent with experimental strain measurements [24,35]. For the examined two coarse grains, “Grain 1” has limited basal slip and nearly no non-basal slip, which manifests its hard-deformed feature. Stress concentration occurs at edge of the grain but hardly penetrates into the interior. “Grain 2”, on the other hand, undertakes large deformation, denoting by the formation of many shear bands inside the grain. As plastic deformation is mainly induced by basal slip, the stress of the grain is small. Therefore, whether in hard or soft orientations, the primary α-Mg solids with larger grain size get smaller stress and bear smaller load. This point can be confirmed by the results of LI et al [36].

In summary, the strength change of the thixomolded AZ91D alloy with primary α-Mg solids origins from two mechanisms. Firstly, the primary α-Mg solid has a large grain size and the decrease of its amount leads to fine grain strengthening. Secondly, with the help of CPFEM simulation, it has been demonstrated that coarse grains in the mixed grain material bear smaller load even in hard orientations. Unraveling the synergy strengthening mechanism helps to deepen the understanding about the mechanical performance of the mixed-grained materials. It is noted that the relationship between the yield strength and fraction of primary α-Mg in Fig. 12 does not follow a regular linear or exponential formulation. This phenomenon is related to the change of grain size of

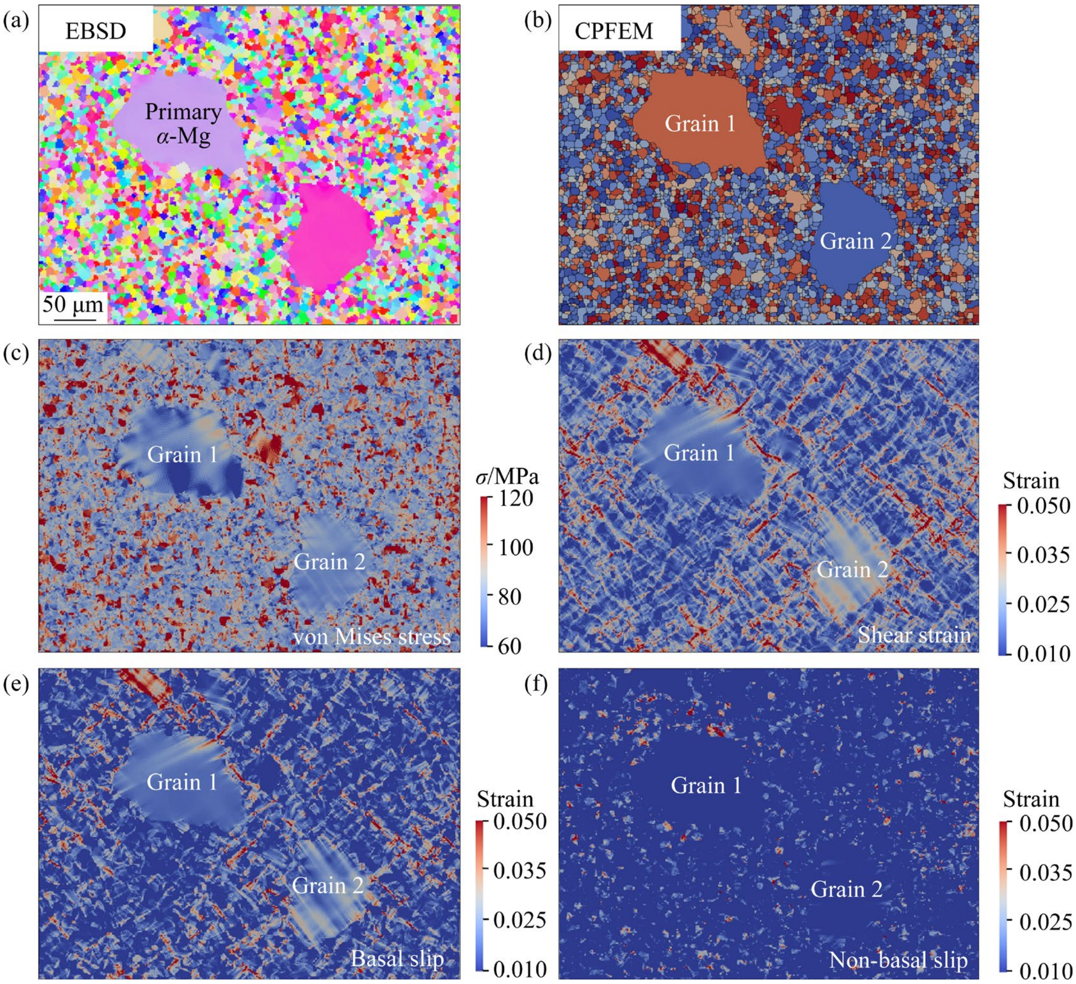

Fig. 13 CPFEM modeling and simulation results: (a) EBSD data for modeling; (b) CPFEM model for hierarchical grain structure; (c) CPFEM simulation results of von Mises stress; (d) Accumulated shear strain from all slip systems; (e, f) Basal slip strain and non-basal slip strain at far-field strain of 0.01, respectively

the primary α-Mg and the non-uniform meso-scale deformation. With the change of injection temperature, both the fraction and grain size of the α-Mg solids change, as denoted by the metallurgical results in Fig. 2. It results in the variation of fine grain strengthening extent in different temperature conditions. Besides, since grain size of primary α-Mg solids is large while the number of them is small, the orientation of individual coarse-grained α-Mg solid plays an important role in material strengthening.

For the change of ductility with temperature, this study suggests that it is primarily related to internal pores. The sample made at an injection temperature of 620 °C gets the maximum elongation of 7.2%, the smallest number of pores and less significant defect concentration. The thixomolded material with the severest defect concentration gets the worst ductility. The changes of flow characteristics and defect formation mechanism with temperature account for the ductility change. In the 590 °C condition, there are additional defect sources of tearing and detachment; in the 640 °C scenario, defect band forms.

5 Conclusions

(1) AZ91D alloy was fabricated by thixomolding with injection temperatures from 580 to 640 °C. The thixomolded material made at 640 °C has the maximum yield strength of 175 MPa, and the one made at 620 °C gets the largest elongation of 7.2%. The thixomolded alloy has the microstructure feature of hierarchical cells composed of α-Mg matrix and eutectic phase. Large cells consist of coarse-grained primary solids, and small cells are constituted by fine-grained α-Mg formed during solidification.

(2) The yield strength increases as the number of large cells decreases. From the CPFEM simulation, it is identified that primary α-Mg solids get lower stress whether they are in hard or soft orientations. Fine grain strengthening extent and small load-bearing of large cells are internal causes for the strength change.

(3) Internal pores were examined by XCT. Volume fractions of pores are 0.33%, 0.25% and 0.41% for samples fabricated at injection temperatures of 590, 620 and 640 °C, respectively. The minimal quantity and lower concentration of pores account for better ductility. At lower injection temperatures, tearing crack and detachment appear due to high viscosity; at higher injection temperatures, defect bands form due to turbulent melt flow. These are additional crack sources.

CRediT authorship contribution statement

Li-dong GU: Investigation, Resources, Writing − Original draft, Data curation, Visualization; **Xiao-qing SHANG:** Conceptualization, Formal analysis, Funding acquisition, Writing − Review & editing; **Jie WANG:** Methodology, Writing − Review & editing, Validation; **Jun-jun DENG:** Investigation, Resources; **Zhen ZHAO:** Supervision, Conceptualization; **Xiao-qin ZENG:** Supervision, Methodology, Funding acquisition.

Declaration of competing interest

The authors declare that they have no known competing financial interests or personal relationships that could have appeared to influence the work reported in this paper.

Acknowledgments

This work was supported by the National Natural Science Foundation of China (Nos. 51825101, 52001202), and the National Key Research and Development Program of China (No. 2021YFA1600900).

References

[1] WANG G G, WEILER J P. Recent developments in high-pressure die-cast magnesium alloys for automotive and future applications [J]. Journal of Magnesium and Alloys, 2023, 11: 78−87.

[2] EBRAHIMI M, WANG Q D, ATTARILAR S. A comprehensive review of magnesium-based alloys and composites processed by cyclic extrusion compression and the related techniques [J]. Progress in Materials Science, 2023, 131: 101016.

[3] RAMALINGAM V V, RAMASAMY P, KOVUKKAL M D, MYILSAMY G. Research and development in magnesium alloys for industrial and biomedical applications: A review [J]. Metals and Materials International, 2020, 26: 409−430.

[4] LI Gan, QU Wen-ying, LUO Min, CHENG Le, GUO Chuan, LI Xing-gang, XU Zhen, HU Xiao-gang, LI Da-quan, LU Hong-xing, ZHU Qiang. Semi-solid processing of aluminum and magnesium alloys: Status, opportunity, and challenge in China [J]. Transactions of Nonferrous Metals Society of China, 2021, 31: 3255−3280.

[5] GU Li-dong, SHANG Xiao-qing, WANG Jie, DENG Jun-jun, LIU Yu-peng, ZENG Xiao-qin, DING Wen-jiang. Development of high strength and high thermal conductivity semi-solid magnesium alloy by thixomolding process [J]. Solid State Phenomena, 2023, 347: 97−106.

[6] OKAYASU M, FUKUI T. A study of the mechanical properties of a Mg−Al−Zn alloy (AZ91) produced via thixomolding [J]. International journal of Material Forming, 2021, 14: 271−280.

[7] MATHIEU S, RAPIN C, HAZAN J, STEINMETZ P. Corrosion behaviour of high pressure die-cast and semi-solid cast AZ91D alloys [J]. Corrosion Science, 2002, 44: 2737−2756.

[8] QI Ming-fan, KANG Yong-lin, XU Yu-zhao, LI Jing-yuan, LIU Ai-sen. New technique for preparing A356 alloy semisolid slurry and its rheo-diecast microstructure and properties [J]. Transactions of Nonferrous Metals Society of China, 2021, 31: 1868−1884.

[9] ATKINSON H V. Modelling the semisolid processing of metallic alloys [J]. Progress in Materials Science, 2005, 50: 341−412.

[10] GU Li-dong, SHANG Xiao-qing, WANG Jie, ZHAO Zhen, ZENG Xiao-qin, DING Wen-jiang. The influence of SiC−Al_2O_3 reinforcements on the deformation and fracture mechanism of thixomolded Mg-based composite [J]. Journal of Materials Science, 2024, 59: 9892−9907.

[11] CHEN Li-wen, ZHAO Yu-hong, HOU Hua, ZHANG Ting, LIANG Jian-quan, LI Mu-xi, LI Jing. Development of AZ91D magnesium alloy−graphene nanoplatelets composites using thixomolding process [J]. Journal of Alloys and Compounds, 2019, 778: 359−374.

[12] RAUBER C, LOHMÜLLER A, OPEL S, SINGER R F. Microstructure and mechanical properties of SiC particle reinforced magnesium composites processed by injection molding [J]. Materials Science and Engineering: A, 2011, 528(19/20): 6313−6323.

[13] PATEL H A, CHEN D L, BHOLE S D, SADAYAPPAN K. Microstructure and tensile properties of thixomolded magnesium alloys [J]. Journal of Alloys and Compounds, 2010, 496: 140−148.

[14] ZHANG Y F, LIU Y B, CAO Z Y, ZHANG Q Q, ZHANG L. Mechanical properties of thixomolded AZ91D magnesium alloy [J]. Journal of Materials Processing Technology, 2009, 209: 1375−1384.

[15] CZERWINSKI F, ZIELINSKA-LIPIEC A, PINET P J, OVERBEEKE J. Correlating the microstructure and tensile properties of a thixomolded AZ91D magnesium alloy [J]. Acta Materialia, 2001, 49(7): 1225−1235.

[16] ZANDER D, SCHNATTERER C. The influence of

manufacturing processes on the microstructure and corrosion of the AZ91D magnesium alloy evaluated using a computational image analysis [J]. Corrosion Science, 2015, 98: 291−303.

[17] BHAGAVATH S, GONG Z, WIGGER T, SHAH S, GHAFFARI B, LI M, MARATHE S, LEE P D, KARAGADDE S. Role of the local stress systems on microstructural inhomogeneity during semisolid injection [J]. Acta Materialia, 2021, 214: 117015.

[18] SHASTRI H, MONDAL A K, DUTTA K, DIERINGA H, KUMAR S. Microstructural correlation with tensile and creep properties of AZ91 alloy in three casting techniques [J]. Journal of Manufacturing Processes, 2020, 57: 566−573.

[19] YU Wen-bo, MA Chao-sheng, MA Yi-hu, XIONG Shou-mei. Correlation of 3D defect-band morphologies and mechanical properties in high pressure die casting magnesium alloy [J]. Journal of Materials Processing Technology, 2021, 288: 116853.

[20] LI Xiao-bo, GUO Zhi-peng, XIONG Shou-mei. Influence of melt flow on the formation of defect band in high pressure die casting of AZ91D magnesium alloy [J]. Materials Characterization, 2017, 129: 344−352.

[21] QIN Ze-hao, KANG Nan, ZHANG Feng-ying, WANG Zi-hong, WANG Qian, CHEN Jing, LIN Xin, HUANG Wei-dong. Role of defects on the high cycle fatigue behavior of selective laser melted Al−Mg−Sc−Zr alloy [J]. International Journal of Fracture, 2022, 235: 129−143.

[22] MENG L X, YANG H J, BEN D D, JI H B, LIAN D L, REN D C, LI Y, BAI T S, CAI Y S, CHEN J, YI J L, WANG L, YANG J B, ZHANG Z F. Effects of defects and microstructures on tensile properties of selective laser melted Ti_6Al_4V alloys fabricated in the optimal process zone [J]. Materials Science and Engineering A, 2022, 830: 142294.

[23] LI X, XIONG S M, GUO Z. On the tensile failure induced by defect band in high pressure die casting of AM60B magnesium alloy [J]. Materials Science and Engineering: A, 2016, 674: 687−695.

[24] SHANG Xiao-qing, ZHANG Hai-ming, WANG Le-yun, ZHU Gao-ming, CUI Zhen-shan, FU M W, ZENG Xiao-qin. The effect of stress state and strain partition mode on the damage behavior of a Mg−Ca alloy [J]. International Journal of Plasticity, 2021, 144: 103040.

[25] KONDORI B, MORGENEYER T F, HELFEN L, BENZERGA A A. Void growth and coalescence in a magnesium alloy studied by synchrotron radiation laminography [J]. Acta Materialia, 2018, 155: 80−94.

[26] AZGHANDI S H, MOHAMADI W M, ARHATARI B D, ADRIEN J, MAIRE E, BARNETT M R. A rationale for the influence of grain size on failure of magnesium alloy AZ31: An in situ X-ray microtomography study [J]. Acta Materialia, 2020, 200: 619−631.

[27] WANG Zhi-qin, ZHANG Bin, LI De-jiang, FRITZSCH R, ZENG Xiao-qin, ROVEN H J, DING Wen-jiang. Effect of heat treatment on microstructures and mechanical properties of high vacuum die casting Mg−8Gd−3Y−0.4Zr magnesium alloy [J]. Transactions of Nonferrous Metals Society of China, 2014, 24: 3762−3768.

[28] ROTERS F, DIEHL M, SHANTHRAJ P, EISENLOHR P, REUBER C, WONG S L, MAITI T, EBRAHIMI A, HOCHRAINER T, FABRITIUS H O, NIKOLOV S, FRIÁK M, FUJITA N, GRILLI N, JANSSENS K G F, JIA N, KOK P J J, MA D, MEIER F, WERNER E, STRICKER M, WEYGAND D, RAABE D. DAMASK—The Düsseldorf advanced material simulation kit for modeling multi-physics crystal plasticity, thermal, and damage phenomena from the single crystal up to the component scale [J]. Computational Materials Science, 2019, 158: 420−478.

[29] SALEM A A, KALIDINDI S R, SEMIATIN S L. Strain hardening due to deformation twinning in α-titanium: Constitutive relations and crystal-plasticity modeling [J]. Acta Materialia, 2005, 53: 3495−3502.

[30] WANG Le-yun, HUANG Zhong-he, WANG Hua-miao, MALDAR A, YI S, PARK J S, KENESEI P, LILLEODDEN E, ZENG Xiao-qin. Study of slip activity in a Mg−Y alloy by in situ high energy X-ray diffraction microscopy and elastic viscoplastic self-consistent modeling [J]. Acta Materialia, 2018, 155: 138−152.

[31] ZHU Zhi-guang, HU Zhi-heng, SEET H L, LIU Ting-ting, LIAO Wen-he, RAMAMURTY U, NAI S M L. Recent progress on the additive manufacturing of aluminum alloys and aluminum matrix composites: Microstructure, properties, and applications [J]. International Journal of Machine Tools and Manufacture, 2023, 190: 104047.

[32] CHEN Ting-shu, CHIBA T, KOYAMA M, SHIBATA A, AKIYAMA E, TAKAI K. Hierarchical characteristics of hydrogen-assisted crack growth and microstructural strain evolution in tempered martensitic steels: Case of quasi-cleavage fracture [J]. Metallurgical and Materials Transactions A, 2021, 52: 4703−4713.

[33] GOURLAY C M, LAUKLI H I, DAHLE A K. Defect band characteristics in Mg−Al and Al−Si high-pressure die castings [J]. Metallurgical and Materials Transactions A, 2007, 38: 1833−1844.

[34] ZHANG Zhi, ZHANG Jing-huai, WANG Wen-ke, LIU Shu-juan, SUN Bin, XIE Jin-shu. Unveiling the deformation mechanism of highly deformable magnesium alloy with heterogeneous grains [J]. Scripta Materialia, 2022, 221: 114963.

[35] SHANG Xiao-qing, ZHANG Hai-ming, CUI Zhen-shan, FU M W, SHAO Jian-bo. A multiscale investigation into the effect of grain size on void evolution and ductile fracture: Experiments and crystal plasticity modeling [J]. International Journal of Plasticity, 2020, 125: 133−149.

[36] LI Yang-qi, ZHANG Hai-ming, SHANG Xiao-qing, LIU Ming-xiang, ZHAO Shi-lin, CUI Zhen-shan. A multiscale investigation on the preferential deformation mechanism of coarse grains in the mixed-grain structure of 316LN steel [J]. International Journal of Plasticity, 2022, 152: 103244.

层级式胞状结构和内部孔隙对触变成形 AZ91D 镁合金力学性能的影响

谷立东[1]，尚晓晴[1,2]，王 杰[1]，邓俊钧[3]，赵 震[4]，曾小勤[1,5]

1. 上海交通大学 材料科学与工程学院 轻合金精密成型国家工程研究中心，上海 200240；
2. 上海交通大学 巴黎卓越工程师学院，上海 200240；
3. 伯乐智能装备股份有限公司，宁波 315801；
4. 上海交通大学 材料科学与工程学院 模具 CAD 国家工程研究中心，上海 200030；
5. 上海交通大学 金属基复合材料国家重点实验室，上海 200240

摘 要：研究了触变成形 AZ91D 合金的显微组织和内部缺陷特征对其力学性能的影响。在 580~640 ℃的触变成形温度下制备了测试样品。使用 X 射线断层扫描技术观察样品内部孔隙，采用晶体塑性有限元模拟对样品进行变形分析。显微组织表征结果表明，半固态触变成形制备的合金具有多层级的胞状组织，α-Mg 基体与周围的共晶相组成了结构胞。随着注射温度的升高，大胞的含量减少，材料强度提升。强度变化机制在于粗晶即使在硬取向下也承受较小的应力。在 620 ℃中等温度制备的样品具有最高的伸长率、最少的孔隙数量和较低的孔隙局部聚集程度。低注射温度下所形成的分离和撕裂以及高注射温度下形成的缺陷带是材料内额外的裂纹源，它们使材料的塑性劣化。

关键词：AZ91D 镁合金；制备工艺；胞结构；孔隙；强度；塑性

(Edited by Wei-ping CHEN)